On the estimation of unsteady aerodynamic forces and wall spectral content with immersed boundary conditions

Lucas Manueco, Pierre-Elie Weiss, Sébastien Deck

Highlights

- Comparison of two approaches for unsteady load computation on Immersed Boundaries
- Extended presentation of a procedure to generate meshes of Immersed Boundaries
- The approach is highly validated for two space launcher RANS/LES simulations
- The load computation does not require extra operation and is performed on-the-fly

On the estimation of unsteady aerodynamic forces and wall spectral content with Immersed Boundary Conditions

Lucas Manueco[a], Pierre-Elie Weiss[a,*], Sébastien Deck[a]

[a] *ONERA, The French Aerospace Lab, F-92190 Meudon, France*

Abstract

Immersed boundary conditions (IBC) have become a practical tool to simplify the meshing process for the simulation of complex geometries in CFD. This approach has reached a sufficient level of maturity to allow the simulation of compressible high Reynolds number flows. However, the access of physical quantities at the immersed wall is far from being straightforward. This paper provides two methods for the reconstruction of fluctuating wall quantities relying on the creation of explicit watertight surface meshes of the immersed boundary. These surface meshes are used for the investigation of highly unsteady compressible flows of two generic space launcher afterbody configurations using Zonal Detached Eddy Simulation (ZDES). Since the flows are massively separated, the side load arising from the pressure is mainly responsible for the global load unsteadiness. Therefore, in the present study the focus is put on the accuracy of the wall pressure reconstructed on immersed boundaries and compared to validated numerical simulations using a classical body-fitted approach and experimental data. The numerical results demonstrate the ability of the present approaches to accurately capture the global load fluctuation around both afterbody configurations. Moreover, the IBC surface meshes simplify the overall post-processing operations and allow the extraction of wall quantities for unsteady simulation at low computational cost. This last feature has been

*Corresponding author
Email address: peweiss@onera.fr (Pierre-Elie Weiss)

used for the spectral analysis on IBC surfaces which reproduced successfully the location and the intensity of the pressure fluctuation.

Keywords: Zonal Detached Eddy Simulation, Hybrid RANS/LES, Immersed Boundary, High Reynolds number, Fluctuating pressure field, Aerodynamic forces

1. Introduction

1.1. Context

Simulation tools play an increasingly important role in aeronautics and enhancing their capabilities for unsteady flow simulations on complex geometries is considered as a major objective in the field. On the turbulence modelling side, hybrid RANS/LES methods are now widely acknowledged as good candidates for technical application to deal with high Reynolds number turbulent flows [46, 43, 16]. However, the design of a proper RANS/LES grid is by far not trivial as the grid cell sizes control the ratio between modelled and resolved turbulence. In addition, the existence of different flow phenomena (*e.g.* massively separated flows, attached boundary layers, etc) places often additional conflicting demands on the grid.

In this framework, the time-honored multiblock structured grid strategy remains an interesting solution for semi-complex geometries due to its computational efficiency and its accuracy. However, the time and level of expertise needed for the design of a proper structured grid increase dramatically with the complexity of the geometry. The emergence of unstructured grid strategies is a direct consequence of this limitation. This later strategy has shown its ability to simplify the grid generation process considerably. Nevertheless, this improvement comes with an increased computational cost and a reduced control over the grid quality[26]. Thus, various numerical techniques emerged in the past decades to improve the capability of structured grids to handle complex geometries while limiting the initial effort required for the grid generation.

Table 1: Simulations with global load computation on IBC according to their level of validation as described by Sagaut and Deck [43]. 0 : instantaneous flowfield visualization, 1: integral forces, 2: mean aerodynamic field, 3: second-order statistics, 4 and 5: one and two point spectral analysis, 6: higher order and time-frequency analysis. Acronyms of the test cases are given in Table 2.

Authors	Applications	Regime	Flow	Reynolds	Mach	Turb. Mod.	Validation
Wang et al. [55]	WP	Compr.	Unsteady	4×10^6	0.3	-	1
Mizuno et al. [33]	MS	Compr.	Unsteady	300	0.3	DNS	0-1
Tamaki and Imamura [50]	WP	Compr.	Steady	2.26×10^6	0.847	RANS	1-2
Balaras [1]	CC	Incompr.	Unsteady	300	-	LES	0-1-2-3
Fadlun et al. [22]	CC	Incompr.	Steady	1000	-		0-1-2
Meyer et al [31]	CC	Incompr.	Unsteady	3900	-	LES	0-1-2-3-4
Nam and Lien [37]	CC	Compr.	Unsteady	2×10^5	1.7	LES	0-1-2-3
Yang and Balaras [63]	MCC	Incompr.	Unsteady	185	-	LES	0-1-2
Tullio et al. [13]	CC, HCC, S / CC, WP	Compr.	Steady	<100 / 6.2×10^6	-/< 1.7	RANS	1-2
Meyer et al. [30]	CC / SC	Incompr.	Unsteady	< 3900	-	LES	0-1-2-3
Cristallo and Verzicco [11]	RV	Incompr.	Unsteady	$< 10^5$	-	LES	0-1-2-3
Tyacke et al. [52]	CJNN	Compr.	Unsteady	3×10^6	-	RANS/LES	0-2-3
Bernardini et al. [2]	WP, CC, S, BFS, RLG	Incompr.	Unsteady	$< 1.1 \times 10^6$	<0.2	RANS/LES	0-1-2-3-4
Tyliszczak and Ksizyk [53]	WC, S	Incompr.	Unsteady	≤ 6700	-	LES	0-1-2-3
Specklin and Delaur [47]	C,STM	Incompr.	Unsteady	$\leq 5.18 \times 10^4$	-	RANS/LES	0-1-2-3
Dairay et al. [12]	P, Ch	Incompr	Unsteady	< 19000	-	LES	0-2-3

Among these methods, Immersed Boundary Methods or Conditions (IBM/IBC) have encountered growing interest and success in the past decades. The term IBC gathers in practice a wide range of methodologies characterised by their capability to impose a wall condition without body-conforming meshes. These methods have allowed to dramatically improve the capacity of structured solvers to simulate complex geometries. Thus, they have become a standard addition to structured solvers [34, 22, 29, 10]. As an example, Cartesian grid methods [4, 49, 8] and Lattice Boltzmann Methods [44, 62] rely almost entirely on IBC for the application of wall boundary conditions. In a different spirit, Weiss & Deck [59] have demonstrated that coupling locally IBC in a structured grid framework together with advanced turbulence modelling offers a very interesting alternative to simulate unsteady turbulent flows on complex geometries.

Though the "standard" IBC methodology is increasingly recognized as a

Table 2: List of acronyms of Table 1.

Acronym	Full denomination
CC	Circular Cylinder
Ch	Channel
CJNN	Coaxial Jet Noise Nozzle
HCC	Heated circular cylinder
MCC	Moving circular cylinder
MS	Moving sphere
P	Pipe
RV	Road vehicle
S	Sphere
SC	Square cylinder
STM	Stirred tank mixer
WC	Wavy Channel
WP	Wing profile

mature approach, the mismatch between the computational grid and the effective wall boundary dramatically limits the accurate analysis of wall-fluctuating quantities which are essential to compute the aerodynamic forces. Indeed, table 1 gathers a set of published works using the IBC technique together with their level validation. One can note that the computation of integral forces is mainly limited to steady-flow configurations or very simple geometries, whereas a spectral analysis on wall fluctuating quantities is rarely addressed by the authors. This may appear paradoxical since the development of IBC is precisely motivated by their potential capability to predict the fluctuating field in complex configurations.

Hence, the main objective of this work is to introduce dedicated methods to extend the capability of IBC methods to permit the analysis of unsteady wall quantities and especially aerodynamic forces. Let us be reminded that the global aerodynamic load induced by pressure P and viscous stresses $\boldsymbol{\tau}$ acting on a solid surface S is given by:

$$F_i = \int_S \underbrace{(\boldsymbol{\tau}_{ij} - P\delta_{ij})}_{(a)} \underbrace{n_j dS}_{(b)} \tag{1}$$

The calculation of Eq (1) requires the knowledge of the stresses (term (a)) acting on the oriented wall surface (term (b)). While these quantities can be easily computed on body-fitted grids knowing the boundary condition, their knowledge is by far not trivial in an IBC context. The objective of this article is to present a general method to assess these two quantities (*i.e.* (a) and (b)) in order to compute the unsteady integral aerodynamic forces on-the-fly on immersed bodies.

The paper is organised as follows: in section 2 we first remind the basis of the IBC framework before presenting the new methodologies and algorithms used

for the study of wall quantities and especially for the assessment of unsteady aerodynamic loads. Section 3 is dedicated to the descriptions of the numerical methods. Finally, in section 4 the methods are finally assessed on two geometries of increasing complexity and representative of a launcher afterbody. Numerical results obtained with IBC are compared both with the available experimental data and the reference body-fitted simulations.

2. Representation of Immersed Surfaces

Since the first work of Peskin [41], Immersed Boundaries (IB) have been widely used in the past decades in order to introduce solids in non-body-fitting grids. The boundary forcing is achieved through the addition of extra terms on the continuous or on the discrete form of the governing equations. In particular, the discrete forcing IB methods have been acknowledged for their capacity to simulate rigid bodies at high Reynolds numbers as emphasized by Mittal and Iaccarino [32].

The main idea of discrete forcing immersed boundary methods is to create the effect of an object in the flow through the application of source terms in near-wall regions cells, named IB forcing points. As depicted in figure 1, near-wall solid [24, 38] or fluid cells [64, 25, 5, 65] can be chosen as forcing points. Moreover, in the particular framework of finite-volume methods, the forcing can also be achieved through the direct manipulation of the numerical fluxes at the faces between solid and fluid cells [7, 51]. Finally, the number of forcing point layers depends on stencil used for the spatial discretisation scheme during the simulation [42].

A reconstruction approach, using near-wall fluid cells is generally used to compute the forcing point source terms. For each forcing point, the conservative variables are reconstructed on a point in the wall-normal direction. Then, the source terms are set to enforce the boundary condition on the immersed solid (i.e. no-slip adiabatic wall). As represented in figures 2 and 3, the immersed

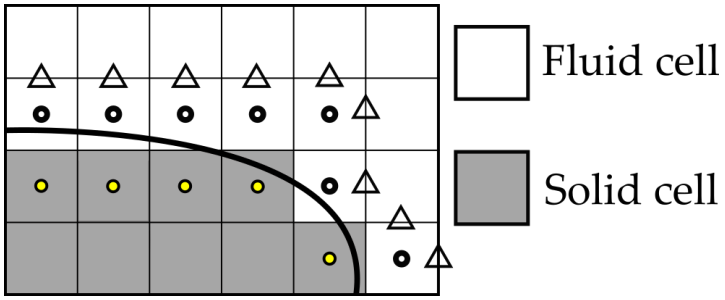

Figure 1: Representation of various possibilities of forcing points (FP) for IBC. ●: Inside solid imposition , ○: outside solid imposition, △: face imposition.

boundary is enforced at only one point, here called Wall Point (WP), per forcing point. In the general case, the location of wall points does not match a point of the computational grid. Therefore, the access to wall quantities on IB is not straightforward and requires dedicated procedures. Since the wall points are independent, the procedural generation of an integration surface for equation (1) remains a major problem to permit global load calculations on IB.

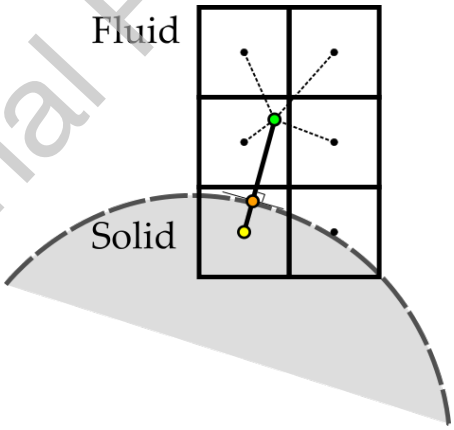

Figure 2: Representation of the interpolation procedure for IBC. ●: Interpolation Points (IntP). ●: Wall Points (WP). ●: Forcing Points (FP) inside the solid.

Tamaki and Imamura [51] used a far-field approach for the computation of the global load on immersed boundaries. This type of approach has been successfully used to assess the global load for steady simulations. Nevertheless, the

extension to unsteady flow requires the calculation of volume terms over a large computational domain. Another solution was recently proposed by [3]. They proposed to interpolate the near-wall quantities on the initial geometry (S_{ref}). This approach has been applied for simple configurations and shows the influence of the interpolation scheme used for the reconstruction. In the present work two approaches without interpolation procedures are proposed for the evaluation of aerodynamic forces on immersed boundaries with discrete forcing. The first approach is based on a stepwise approximation (see Fig. 3) of the immersed boundary for the assessment of the global load. For the special case of stepwise immersed boundaries [22, 6] this solution will lead to an exact reconstruction of the surface. The second approach relies on a precise reconstruction of the IB surface to minimize the error from term (b) in equation (1). Both methods are designed to generate watertight surfaces and to require minimum operations during CFD simulations for an on-the-fly assessment of unsteady aerodynamic forces. In addition, they are independent of the IB formulations and can be used with any discrete forcing methods.

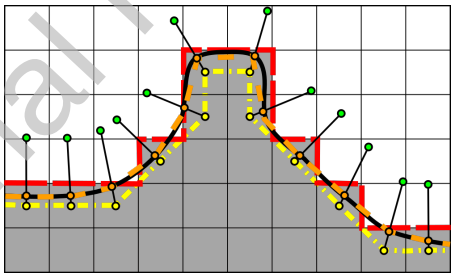

Figure 3: Scheme of the influence of the discretization on the geometry representation. Exact geometry (S_{ref}). Inside Solver Geometry (S_{ISG}). Intermediate surface ($Sint_V$). Stepwise surface ($S_{F/S}$). : Interpolation Points (IntP). : Wall Points (WP). : Forcing Points (FP) inside the solid.

2.1. Stepwise oriented surface approximation

The access to the IB wall content, represented by the wall points, requires additional operations that are unnecessary to enforce the IBC. Hence, the present

approach is designed to assess aerodynamic forces on IB with only marginal additions to CFD solvers. Assuming the knowledge of the grid and the cell states (i.e. fluid or solid), a stepwise surface $S_{F/S}$, depicted in figure 3, can be easily created, through the summation of $\Delta S_{F/S}$, the cell faces between fluid and solid cells. In the particular case where $S_{F/S}$ is aligned with the IB (i.e. S_{ref}) , the representation of the surface would be the true representation of the boundary. Even for unaligned geometries, Mizuno et al. [33] showed that such an approach provides a quite accurate evaluation of global load for the direct numerical simulation of a moving sphere.

In the framework of Finite Volume (FV) methods, the conservative variables are reconstructed at the cell faces during the computation of the numerical fluxes. Therefore, their assessment on the $\Delta S_{F/S}$ is already computed during the simulation and can be used to approximate the wall-stress. Hence, the new equation for the computation of aerodynamic forces on the stepwise surface reads as :

$$F_i \simeq \sum_{l}^{nbr\ F/S} \underbrace{(\boldsymbol{\tau}_{ij} - P\delta_{ij})_{F/S_l}}_{(a)} \underbrace{(n_j \Delta S)_{F/S_l}}_{(b)} \tag{2}$$

Where $nbr\ F/S$ is the number of faces between fluid and solid cells. This simple approach requires only a minor implementation effort, is computationally inexpensive for FV methods and provides a proper evaluation of aerodynamic forces as illustrated later in section 4. The procedure used to compute (2) is detailed in Algorithm 1.

Algorithm 1 Stepwise surface reconstruction

During the computation of the FV fluxes

for Each face **do**

  if the present face is between a fluid and a solid cell **then**

    $\boldsymbol{\tau}_{ij} - P\delta_{ij}$ is computed using the face values (term (a))

    $\mathbf{n}\Delta S$ of the face is used for the evaluation of the local surface (term (b))

  end if

end for

2.2. Immersed boundary surface reconstruction

As reminded in section 2, the IB is enforced at the IB wall points (see Fig. 3). During the computation, the forcing points flow variables are computed using the chosen IBC formulation to create the effect of the boundary inside the fluid. Using the same boundary formulation, the computation of the flow variables at the wall points is straightforward and provides a direct access to wall quantities on IB. Therefore, the evaluation of the wall stress on the immersed boundary can be obtained without any further interpolation and approximation. The main bottleneck of this idea lies in the computation of a consistent oriented surface contribution $\mathbf{n}\Delta S$ for each wall points to assess aerodynamic forces.

In the framework of Cartesian grid solvers with face-forcing IBC, Capizzano [9] proposed an efficient algorithm to create a surface mesh between IB wall points that could eventually be used for visualisation purposes and global load computations.

This surface, illustrated in figure 3, is created using the IB wall points (see Fig. 2) and is referred here to as S_{ISG} where ISG stands for Inside Solver Geometry. It is supposed to correspond to the surface actually introduced inside the solver by the immersed boundary method. The ISG is particularly adapted if the characteristic length Δl_S of the elements discretizing the exact surface

geometry S_{ref} is equal or greater than Δx, the characteristic length of a grid cell. In this case, where $\Delta l_S \geq \Delta x$, the resulting surface S_{ISG} would match the immersed geometry. However, for $\Delta l_S << \Delta x$ the ISG could misrepresent highly curved geometries as depicted in figure 4. Moreover, as stated in section 2, multiple layers of forcing points may be required to create the IB. Nonetheless, S_{ISG} is created using the first layer of forcing points and does not take into account the other layers. As a consequence, the geometrical details brought by the other forcing point layers, and their related wall points, are not considered during the creation of S_{ISG}.

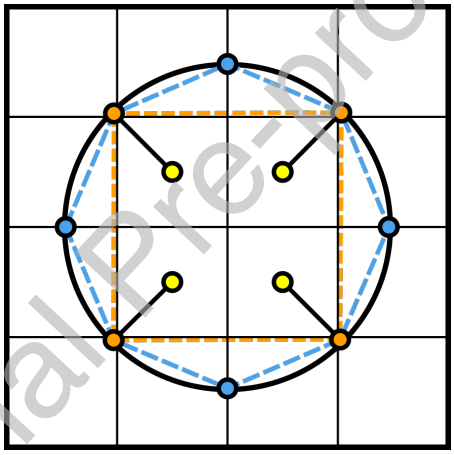

Figure 4: Immersed boundary surface reconstruction of a 2D cylinder. Inside Solver Geometry (ISG). Projected Inside Solver Geometry (PISG). Exact geometry. : Wall Points (WP). : Forcing Points (FP) inside the solid. : Construction Points for S_{PISG}.

A new approach, called Projected ISG (PSIG) has been developed to reduce the error on the surface approximation while keeping possible the direct evaluation of the wall stress. The approximation made on the reconstructed surface is controlled through successive correction steps. Since the creation of the new surface relies on the ISG surface, the algorithm of Capizzano [9] has been adapted to IB methods based on inside and outside forcing points.

As proposed by Capizzano [9] the connectivity between vertices and cells can be advantageously used to create this first surface. For every vertex V around the immersed boundary the following operation is performed to create an intermediate surface , $Sint_V$ (see Fig. 3), between Forcing Points (FP) :

$$\forall FP \in (\{C_V\} \cap \{K_V\}) \Rightarrow FP \in \{Sint_V\} \tag{3}$$

Where $\{C_V\}$ is the set of cells sharing the vertex V and where $\{K_V\}$ represents a complementary test required to avoid wrong connections for thin IB as presented in figure 5. Hence, $\{K_V\}$ is defined as the set of cells sharing a cell face with a fluid cell included in $\{C_V\}$. For outside forcing points, $\{K_V\}$ is defined as the set of cells sharing a cell face with a solid cell included in $\{C_V\}$.

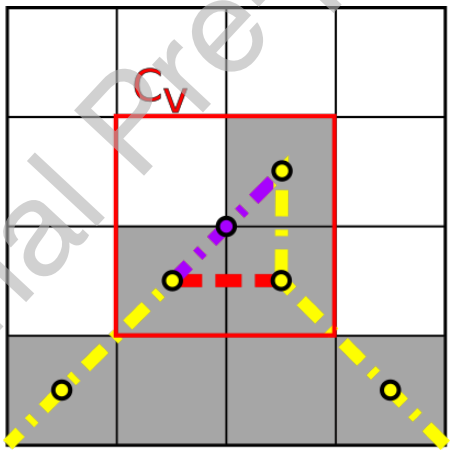

Figure 5: Illustration of wrong connection detection for the generation of the immersed boundary surface mesh. : Forcing points (FP) inside the solid. : Vertex of interest. : FP connections. : Erroneous connection. : Connection created.

Finally, the coordinates of the forcing points are replaced by their related Wall Points (WP) to create the ISG surface.

$$FP \in \{Sint_V\} \Rightarrow WP \in \{S_{ISG}\} \tag{4}$$

For structured meshes, three to four wall points are classically linked by vertices. The surface between these points is decomposed into triangles to compute the local surface value ΔS_{ISG} associated to an IB wall point as depicted in figure 6. Therefore, the resulting force applied on an IB can be computed as follows:

$$F_i \simeq \sum_{l}^{FP\ nbr} \underbrace{(\tau_{ij} - P\delta_{ij})_{WP_l}}_{(a)} \underbrace{(n_j \Delta S_{ISG})_{WP_l}}_{(b)} \tag{5}$$

Where $FP\ nbr$ is the number of forcing points.

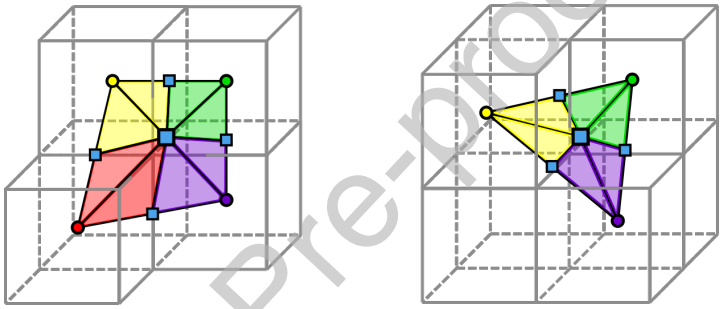

Figure 6: Decomposition of S_V between the immersed boundary wall points. circles : IB wall points / squares : construction points

In the cases where $\Delta l_S << \Delta x$, additional operations are realized in order to improve the accuracy of S_{ISG}. This new surface S_{PISG} is obtained via successive refinement and projection of the triangles obtained in figure 6. First of all, the construction points, used to decompose the surfaces in triangles, are projected on S_{ref}. Then, the triangles can be successively decomposed as shown in figures 4 and 7 and the additional construction points are projected on S_{ref}. Each decomposition level reduces the size Δl_S of the reconstructed surface elements and reduces the error during the reconstruction process. This recursive decomposition can be performed as many times as required until convergence of the reconstructed surface. Finally, for each wall point, the locally oriented surface $\mathbf{n}\Delta S_{(P)ISG}$ is computed through the summation of the triangle surfaces.

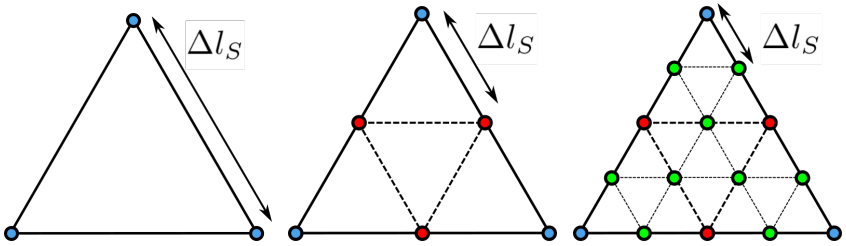

(a) n=0 (b) n=1 (c) n=2

Figure 7: Illustration of the triangle decomposition procedure proceeded three times on the triangulated surface in figure 6.

To assess the accuracy of the present reconstruction approach, several numerical tests have been performed. A sphere has been immersed in a Cartesian grid with a cell size Δx. The relative error, $(S - S_{ref})/S_{ref}$, on the global surface reconstruction has been plotted in figure 8 for different Δx and for different refinement levels of the PISG surface. The number n represents the level of projection used (i.e. $n = 0$ for the ISG surface, $n = 1$ for the PISG surface without sub-triangle decomposition, $n > 2$ for the PISG surface with n-1 sub-triangle divisions see fig 7). Figure 8 shows the second-order accuracy obtained with both the ISG and the PISG methodologies for $\Delta l_S << \Delta x$. Moreover, the error on the surface representation is clearly reduced for each new subdivision step. Figure 9 reports the same plot for two different Δl_S. The ideally achieved second-order accuracy is not preserved when $\Delta l_S \simeq \Delta x$. In practice, the triangle subdivision process is stopped before this loss of accuracy to avoid the introduction of a large numerical error during the summation of the triangle surface to compute S_{PISG}.

The projection procedure used to generate the PISG surface may appear computationally expensive. The major cost lies in the multiple triangle projections on S_{ref}. This cost can be severely reduced by using kd-trees to partition S_{ref} (see [54] for more information on kd-trees architectures). Moreover, these operations are only performed once before the simulation. The overall procedure is detailed in Algorithms 2 and 3. A simplified procedure has also been

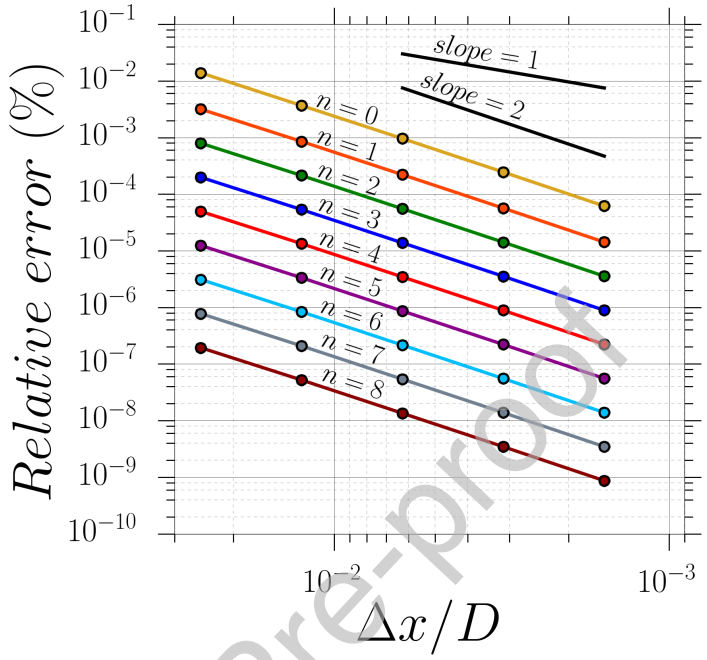

Figure 8: Relative error of the surface reconstruction method against the grid size for different levels n of projection.

developed in order to create a structured surface mesh linking the forcing points and is described in Appendix A. In addition, it is worth mentioning that the surface mesh between IB wall points generated during the creation of S_{ISG} can also be used to extract wall quantities on a surface mesh file. This feature has been presently used to assess the capacity of IB to obtain an accurate single and two-point analysis of the wall fluctuating pressure field (see section 4).

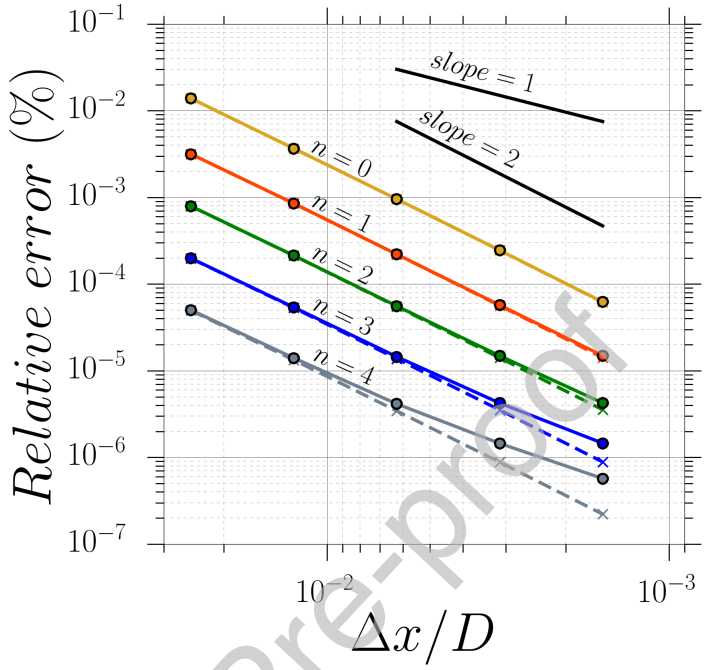

Figure 9: Relative error of the surface reconstruction method against the grid size for different levels n of projection for two different geometrical files. straight line : coarse geometry / dotted line : fine geometry.

Algorithm 2 Creation of S_{ISG}

for each vertex **do**
  The cells linked to this vertex are included in the set V
  for each cell $\in$ V **do**
    if $cell_V \in$ FP **then**
      if $cell_V$ shares a face with a fluid $cell$ $\in$ V **then**
        $cell_V$ is included in $Sint_V$
      end if
    end if
  end for
  The wall points corresponding to the forcing points in $Sint_V$ are included in S_{ISG}
  A surface composed by triangles is formed to compute the oriented surface associated with a wall point
  (Optional) The triangles are split and projected on S_{ref} to create S_{PISG}
end for

Algorithm 3 Global load computation with S_{ISG} and S_{PISG}

At the end of an iteration

for Each IB forcing point **do**

Computation of the flow variables at the corresponding Wall Points

Computation of $\boldsymbol{\tau}_{ij} - P\delta_{ij}$ at the Wall Points (term (a))

(Optional) Storage of the Wall Point values for wall extraction

Computation of the global load using the evaluation of the local wall surface $\mathbf{S}_{(P)ISG}$ (term (b))

end for

3. Numerical method

3.1. Solver description

The present simulations were performed using the FLU3M cell-centred finite volume research code. The validation of this solver has been assessed on various applications for steady and unsteady flow regimes, especially in the framework of space launcher simulations [20, 60, 58, 59, 45, 39]. FLU3M solves the compressible Navier-Stokes equations on multiblock structured grids. The calculations presented in this paper were done using a modified low-dissipation AUSM+(P) scheme developed by Liou [27] for the convective fluxes. A MUSCL reconstruction method is used without limiter to increase the spatial accuracy of this scheme. The gradients for the diffusion fluxes are evaluated using the Green-Gauss method, which is known to be second-order accurate for structured mesh [48]. Finally, the time discretisation is carried out using the implicit and second-order accurate Gear scheme [23] associated to a Newton-type iterative algorithm.

3.2. Zonal Detached Eddy simulation

The ZDES approach developed by ONERA[14, 15] belongs to the family of multiresolution approaches. This hybrid RANS/LES method, based on the Spalart-Allmaras (SA) model, is particularly suited for the study of different

flow topologies within the same simulations as demonstrated by [17]. Indeed, the three specific length scales, or modes, of ZDES (See Eq. (6)) are each optimised for a particular flow topology as illustrated in figure 10. For each ZDES mode, the corresponding length scales is introduced in the Spalart-Allmaras turbulence model by substitution of the wall distance d_w by $\tilde{d}_{ZDES}$ as follows:

$$\tilde{d}_{ZDES} = \begin{cases} d_w & \text{if } mode = 0 \\ \tilde{d}^{I}_{ZDES}(\tilde{\Delta}) & \text{if } mode = 1 \\ \tilde{d}^{II}_{ZDES}(\tilde{\Delta}) & \text{if } mode = 2 \\ \tilde{d}^{III}_{ZDES}(\tilde{\Delta}) & \text{if } mode = 3 \end{cases} \tag{6}$$

where $\tilde{\Delta}$ is the subgrid length scale and is either based on the volume of the cell $\tilde{\Delta} = \Delta_{vol} = (\Delta x \Delta y \Delta z)^{1/3}$ or based on the vorticity $\tilde{\Delta} = \Delta\omega =$ (where S_ω is the averaged cross section of the cell normal to the vorticity vector $\boldsymbol{\omega}$, see [15] for details).

In the present configurations described in section 4.1 the flow separation is caused by a geometrical discontinuity at the end of the upstream cylinder (see Figure 11). Two modes of ZDES have been used in one simulation. The upstream attached flow is modelled by ZDES mode 0, which corresponds to an URANS SA modelling, whereas the downstream separating flow is modelled using ZDES mode 1. Such an approach is selected due to the fact that it allows a higher control on the boundary layer development before the separation point. Downstream the separation point, the mode 1 of ZDES ($\tilde{\Delta}^I = \tilde{\Delta}$) is particularly adapted for the study of massively separated flows. Consequently, d_w is replaced by $\tilde{d}^{I}_{ZDES}$ in the LES regions according to:

$$\tilde{d}^{I}_{ZDES} = min\left(d_w, C_{DES}\tilde{\Delta}^I\right) \tag{7}$$

where $C_{DES} = 0.65$. Given Δ_{vol} has been successfully used for the simulation of space launcher configurations [20, 56, 60] this length scale is chosen in the present study.

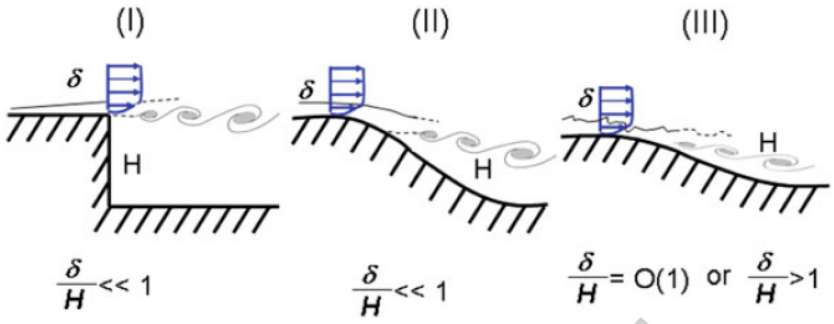

Figure 10: Classification of typical flow problems [15] . I: location of the separation known in advance since fixed by the geometry, II: location of the separation unknown a priori, e.g. induced by a pressure gradient on a curved surface (see also [19]), III: separation strongly influenced by the dynamics of the incoming boundary layer (e.g. WMLES mode).

3.3. Immersed Boundary Condition

The current immersed boundary approach is based on the direct forcing approach developed by Mohd-Yusof [36] and adapted in a finite volume context. This method belongs to the discrete immersed boundary approaches and uses the cells inside the solid as forcing points to enforce the boundary condition. As a result, the IB source terms are imposed in the momentum equations and in the pseudo eddy viscosity transport equation of the Spalart-Allmaras model. Due to the implicit time integration scheme, the IB forcing should require the inversion of a large sparse system during the simulation. In practice, an explicit source term formulation has been adopted which is applied during the inner iteration of the implicit time step. Balaras [1] exhibits that this explicit approach with sub-iterations during the implicit time-stepping shows only slight differences with a fully explicit approach. Thus, during a time step n, the explicit residual R^{n+1} of the momentum equations and the turbulent transport equation is nullified to impose the desired value inside the immersed solid. The discrete formulation of the finite volume system can be written as follows :

$$\frac{3}{2}\Delta\mathbf{W}^{n+1} - \frac{1}{2}\Delta\mathbf{W}^{n} = -\frac{\Delta t}{\Omega}\left(\sum_{l=1}^{6}\left[(\mathbf{F_c})_l - (\mathbf{F_d})_l\right]^{n+1} - \left[\mathbf{T_{ZDES}}\right]^{n+1} - \left[\mathbf{T_{IBC}}\right]^{n+1}\right) \quad (8)$$

where $\mathbf{W}^n$ is the conservative variable vector at the iteration n and $\Delta\mathbf{W}^n = \mathbf{W}^n - \mathbf{W}^{n-1}$, $\mathbf{F_c}$ and $\mathbf{F_d}$ are the convective and the diffusive fluxes, Ω the volume of a cell and $\mathbf{T}$ the source terms for the IB forcing and the ZDES approach. The expression of $\mathbf{T_{IBC}}$ is defined as follows :

$$\mathbf{T_{IBC}} =^t \left(0, tagibc \times f^{n+1}_{\rho u_i}, 0, tagibc \times f^{n+1}_{\rho\tilde{\nu}}\right) \tag{9}$$

with $f^{n+1}_{\rho u_i}$ and $f^{n+1}_{\rho\tilde{\nu}}$ are the sum of the convective and diffusive fluxes for the momentum and the conservative turbulent variable, respectively. The sensor *tagibc* is equal to 1 inside the immersed solid and 0 outside. Further details concerning the implementation and the discretisation of the Immersed Boundary approach can be found in Weiss and Deck [59].

A hybrid body-fitted/IBC approach named Zonal Immersed Boundary Condition (ZIBC) is used in the present work. This methodology has been introduced by Mochel et al. [35] to include a control device in a pre-existing body-fitted simulation. This numerical strategy takes full advantage of its zonal nature by restricting the use of body-fitted approach to the simplest part of the geometry. Therefore, the complex parts of the geometry are taken into account with immersed boundaries to avoid the time-consuming meshing step intrinsic to the generation of structured body-fitted grids.

4. Results and Discussion

4.1. Test Cases

Two generic configurations of space launcher afterbodies are considered to assess the capacity of IB to analyse fluctuating wall quantities. Such geometries are subject to significant pressure fluctuations on the afterbody walls issuing from strong geometrical changes. The first configuration, depicted in figure 11 (a), is designed to reproduce the experimental set-up of Deprés et al. [21] (see also [28]). It consists in two connected cylinders of diameter $D = 100$ mm and $0.4D$, respectively. The length of the larger cylinder has been adjusted to obtain a boundary layer thickness ratio δ/D of 0.2 before the separating point.

Finally, the length L of the smaller cylinder is prescribed to match a L/D ratio equal to 1.2. The second configuration corresponds to a "smooth" Ariane 5 afterbody (i.e. without technological details) represented in figure 11 (b). The smaller cylinder of the first configuration is replaced by the real afterbody geometry and the length of the bigger cylinder is truncated in order to match the ratio of $\delta/D = 0.1$ used in the ZDES simulation performed by Weiss and Deck [57] with a body-fitted grid. For both cases, the Reynolds number based on D has been set to $1.2 \cdot 10^6$, and the corresponding free stream Mach numbers are equal to $M = 0.702$ and $M = 0.8$ for the first and the second cases, respectively.

To assess the capacity of the present IB method to correctly mimic complex geometries without mesh adaptation, both simulations were performed on the same structured curvilinear grid. This grid is the same as in Pain et al. [40] which has been generated using the convergence study performed by Deck and Thorigny [20]. In the configuration 1, the cell faces are aligned with the immersed boundary which corresponds to the most favourable case to evaluate the sole effect of the wall boundary formulation without any bias due to a mismatch between the mesh and the immersed geometry. Conversely, configuration 2 is not aligned with the background mesh and is used to assess the present methodologies on an industrial case.

4.2. Instantaneous Flow Field

Figure 12 presents the main characteristic of the massively separated flow for the second configuration. In both configurations, the abrupt change of geometry at the end of the upstream cylinder generates toroidal structures rapidly converted into three-dimensional structures. Considering that the upstream cylinder is modelled using a body-fitted approach for all simulations and that the influence of the IB condition has not shown any modification on their development, the shear layer structures present the same salient features. As a consequence, the prediction of fluctuating wall quantities on the rear-body is only affected by the boundary condition, either IBC or body-fitted, used to en-

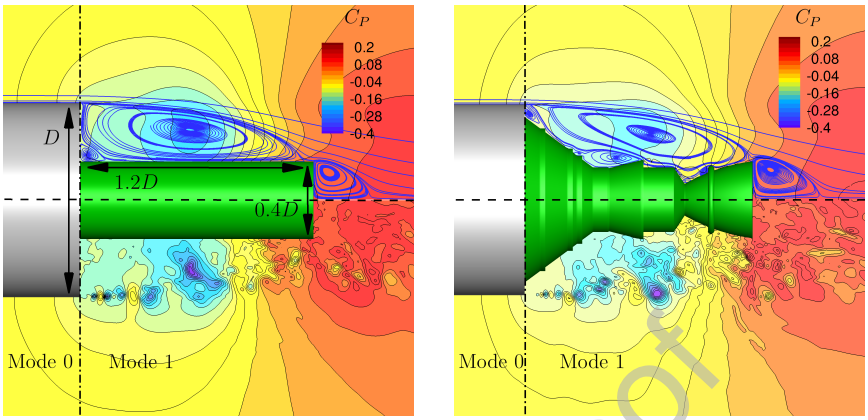

(a) Conf. 1 (b) Conf. 2

Figure 11: Contours of the pressure coefficient C_P and streamlines (upper part: mean flow field, lower part: instantaneous flow field) with characteristic sizes of the geometries and ZDES modes locations. Green parts are modelled using IBC.

force the no-slip condition. Nonetheless, the assessment of this effect is only possible through higher validation levels such as first and second order statistics and spectral analyses.

4.3. First and second-order statistics

The unsteady wall values have been time-averaged during the ZDES simulations. The streamwise evolution of the mean pressure coefficient $C_P = \frac{P-P_0}{q_\infty}$ (where $q_\infty = \frac{1}{2}\rho_\infty U_\infty^2$ is the free-stream dynamic pressure) and the r.m.s pressure coefficient $C_{Prms} = \frac{Prms}{q_\infty}$ at the wall are plotted in figures 13 and 14 for the first and the second configurations, respectively. The longitudinal evolution of C_P allows to identify the recompression phenomenon occurring in the recirculation zone around the afterbodies. A first region between $x/D = 0$ and $x/D = 0.6$ shows a decrease in C_P caused by the acceleration of the backflow. Finally, the end of the afterbodies are subject to a strong recompression due to the impact of the shear layer structures on the surface. The same process is shown for the second configuration with the same intensity. However, the

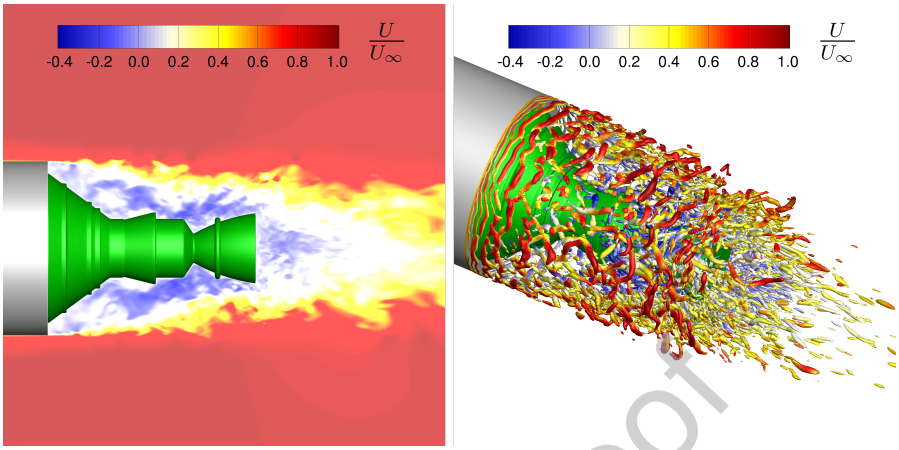

Figure 12: (Left) Longitudinal cut of the instantaneous dimensionless velocity of the ZDES/IBC simulation for configuration 2. (Right) Visualisation of coherent structures via an iso-surface of the dimensionless Q criterion ($Q \cdot D^2/U_\infty^2 = 100$) colored by the dimensionless streamwise velocity component.

abrupt geometrical changes observable at $x/D = 0.65$, 0.8 and 1.0 generate local recompression processes that are well captured by the IBC simulation.

The streamwise evolution of C_{Prms} coefficient for the first configuration shows a good agreement with the experiment of Meliga and Reijasse [28]. The pressure fluctuation levels along with there locations are well-described by the body-fitted and the IB simulations. For this configuration, C_{Prms} increases regularly until $x/D = 0.8$ where a constant value is reached around $C_{Prms} = 0.035$. As in the C_P distribution, the C_{Prms} values for the second configuration is perturbed by the three geometrical changes. The major distribution of the pressure fluctuation is well reproduced in the IB simulation.

To get further into the validation of the IBC simulation, the streamwise mean and rms velocity profiles were plotted at three locations for both configurations. These profiles are located at $X/D = 0.2$, 0.6 and 1.0 and are plotted in figures 15, 16 and 17, respectively. They are chosen to compare the body-fitted and the immersed boundary simulations at different stages of the mixing layer development. Here again, the agreement between the body-fitted and the im-

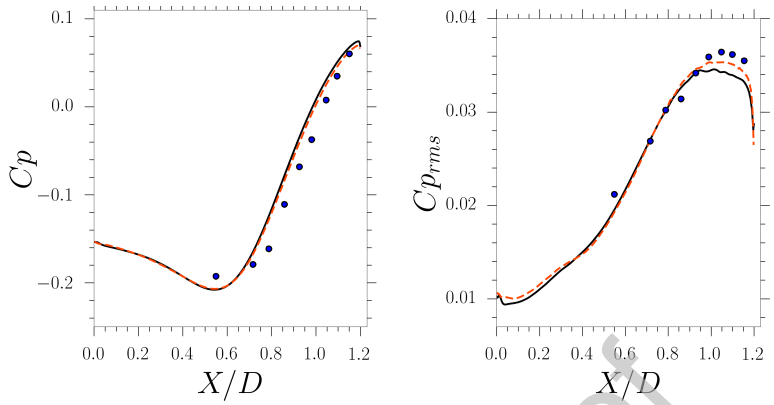

Figure 13: Streamwise evolution of the mean pressure coefficient (Left) and the rms pressure coefficient (Right) at the wall for conf.1. ——: Body-fitted, - - -: Immersed Boundary, •:Meliga et al [28].

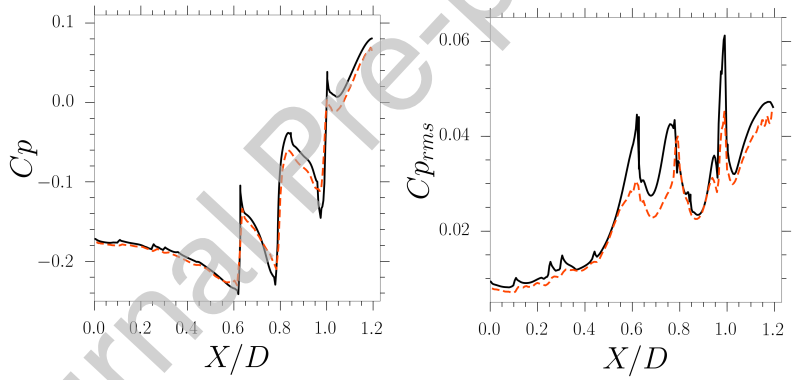

Figure 14: Streamwise evolution of the mean pressure coefficient (Left) and the rms pressure coefficient (Right) at the wall for conf.2. ——: Body-fitted, - - -: Immersed Boundary.

mersed boundary simulations is satisfying. The main discrepancies are located at the early stages of the mixing layer for the rms streamwise velocity for configuration 2 (Fig. 15). Nonetheless, the mean velocity is still mainly retrieved with IBC. At $X/D = 0.6$, a strong backflow reaching 40 % of the free stream velocity is equally predicted for both configurations. Finally, for the intense velocity fluctuations at this location and at $X/D = 1.0$ (Figs. 16 and 17) the

two methods show only small discrepancies.

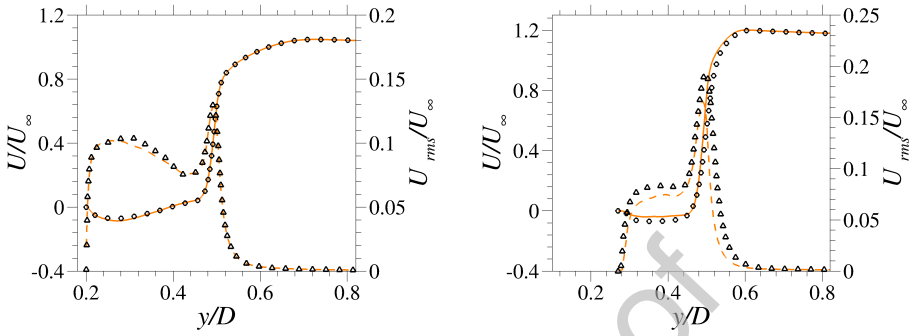

(a) Configuration 1 (b) Configuration 2

Figure 15: Dimensionless streamwise mean velocity profile U/U_∞ (——: Immersed Boundary, o: Body-fitted) and Dimensionless streamwise rms velocity profile U_{rms}/U_∞ (- - -: Immersed Boundary, △: Body-fitted) at $X/D = 0.2$.

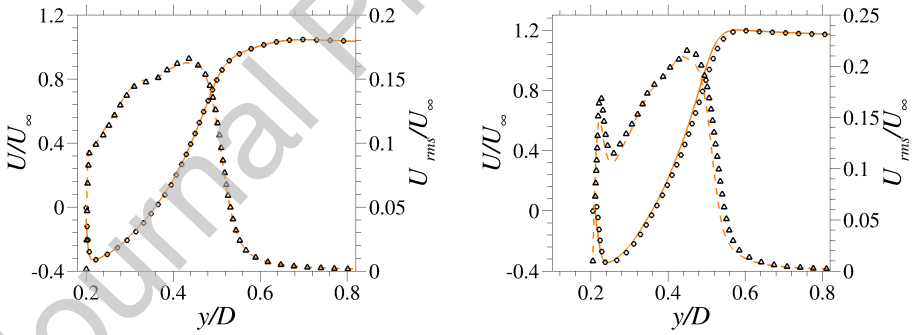

(a) Configuration 1 (b) Configuration 2

Figure 16: Dimensionless streamwise mean velocity profile U/U_∞ (——: Immersed Boundary, o: Body-fitted) and Dimensionless streamwise rms velocity profile U_{rms}/U_∞ (- - -: Immersed Boundary, △: Body-fitted) at $X/D = 0.6$.

4.4. Unsteady aerodynamic loads

Due to the strong geometrical change at the end of the upstream cylinder, the flow around the afterbodies is massively separated. The resulting wall pressure

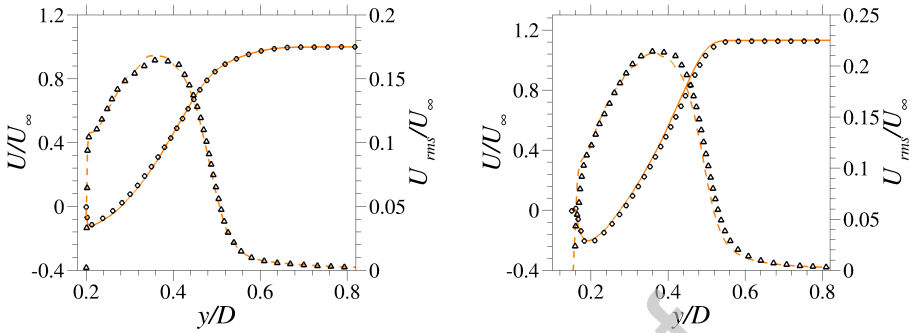

(a) Configuration 1

(b) Configuration 2

Figure 17: Dimensionless streamwise mean velocity profile U/U_∞ (——: Immersed Boundary, o: Body-fitted) and Dimensionless streamwise rms velocity profile U_{rms}/U_∞ (- - -: Immersed Boundary, ▲ : Body-fitted) at $X/D = 1.0$.

fluctuation leads to non-axisymmetric unsteady repartition of the instantaneous pressure field on the afterbody. Since the flows are massively separated, the study is limited to the prediction of the side load arising from the pressure. The time history of the pressure loads applied on the afterbody parts of the configurations (see parts in green in figure 11) have been sampled during the simulation over a total duration of 200 ms. Figures 18 (a) and (b) provide a polar plot of the two components of the dimensionless side load $Cf_z = F_z(t)/(q_\infty \pi D^2/4)$ and $Cf_y = F_y(t)/(q_\infty \pi D^2/4)$ for configurations one and two, respectively. These loads, corresponding to the forces which apply normally to the free stream direction, are normalised by the dynamic pressure q_∞ and $S_{ref} = \frac{\pi D^2}{4}$. The random character of this load fluctuation can be assessed through its statistical properties using the confidence ellipse of the bidimensional variables defined by $\tilde{F} = [F_y, F_z]^t$. As described by Deck and Nguyen [18], the confidence ellipse with $\alpha = 95\%$ includes 95% of the observation of $\tilde{F}$. The shape and the size of this ellipse reflect the distribution and the intensity of the dynamic load phenomenon.

For the first configuration, the stepwise and the accurate approaches de-

scribed in section 2.2 give the same results with an underlying mesh conforming the geometry of the afterbody. Moreover, the intensity and the repartition of the global load of the IB simulation are coherent with the body-fitted results. Thus, the IB formulation is able to reproduce a no-slip condition as a classical boundary condition would do. For the second configuration, the results do not converge to the same confidence ellipses (see figure 18 (b)) suggesting the accurate reconstruction of the surface is of primary importance in the estimation of the physical quantities at the wall.

As a consequence, during the same simulation, the global load has been computed with several IB surface reconstructions. The statistical properties of the resulting dynamic loads are reported in table 3 along with the computational cost associated with the creation of the integration surface. Due to the axisymmetry of both configurations the resulting ellipses are supposed to converge to a centered circle (i.e. $\overline{Fy} \simeq \overline{Fz} \simeq 0$ and $\sigma_{Fz}/\sigma_{Fy} = 1$). This can be analysed through the ratio between the standard deviation of Fz and Fy which is also confirmed by the fact that the mean values of the two components of the load are $\overline{Fy} \simeq \overline{Fz} \simeq 0$. The intensity of the global load can, therefore, be assessed through the radius of the circle.

As explained in section 2, the wall stress on S_{ISG} and S_{PISG} is computed without approximation or additional interpolation procedures. As a consequence, the discrepancies between the global load is only due to the refinement of the integration surface. As shown in table 3, the confidence ellipse properties converge after only 12 refinement levels of the S_{PISG} surface and improves greatly the assessment of the dynamic load. The preprocessing time required to create S_{PISG} may seem prohibitive but its generation is highly parallelized. On the other hand, the stepwise approach is shown to overestimate the global load on the second configuration. Nonetheless, this approach does not require preprocessing operations and can therefore be used for a quick estimation of the load.

The analysis of this phenomenon can be developed through the analysis of

Table 3: First and second order statistical properties of the dynamic load integrated with different reconstructed surfaces on configuration 2 during 200 ms of simulation along with the time required to generate these surfaces, $\overline{R}$ denotes the radius of the circle in the case of axisymmetric flows.

	σ_{Fz}/σ_{Fy}	$\overline{Fy}$	$\overline{Fz}$	$\overline{R}$	S/S_{ref}	Time (s)
Body-Fitted	0.9941	-5.473E-5	7.213E-5	6.743E-3	1.0	$\emptyset$
Stepwise	0.9839	-9.581E-5	1.538E-5	6.832E-3	1.219	$\emptyset$
S_{ISG}	0.9809	-4.710E-5	-1.629E-6	6.560E-3	0.980	6.43
S_{PISG} $n=1$	0.9862	-6.762E-5	3.114E-5	6.582E-3	0.984	13.37
S_{PISG} $n=5$	0.9862	-5.361E-5	-4.331E-6	6.648E-3	0.992	128.40
S_{PISG} $n=8$	0.9862	-4.969E-5	9.600E-6	6.648E-3	0.994	1133.92
S_{PISG} $n=12$	0.9862	-4.249E-5	2.097E-5	6.648E-3	0.995	18839.98
S_{PISG} $n=16$	0.9862	-3.793E-5	2.502E-5	6.648E-3	0.995	329378.49

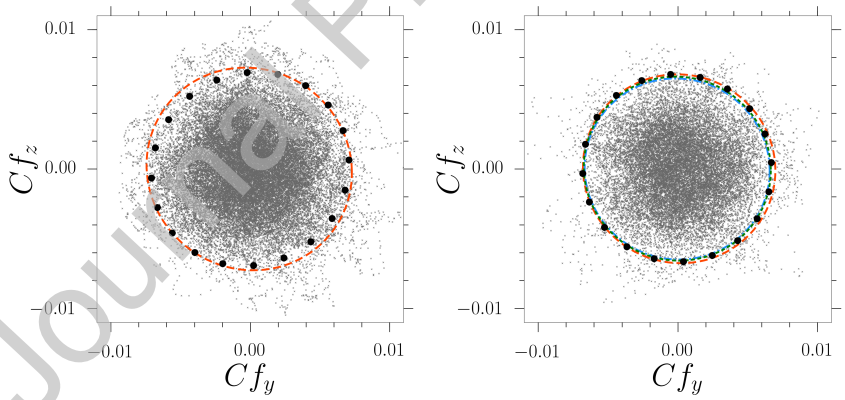

(a) Configuration 1 (b) Configuration 2

Figure 18: Plot of the 95% confidence ellipses obtained with the present simulations. ——: Body-fitted, - - -: Stepwise approach (IB), - - -: S_{ISG} (IB), - - -: S_{PISG} (IB). ●: global load values (IB).

G_{F_y} and G_{F_z} which represent the Power Spectral Density (PSD) of the aerody-

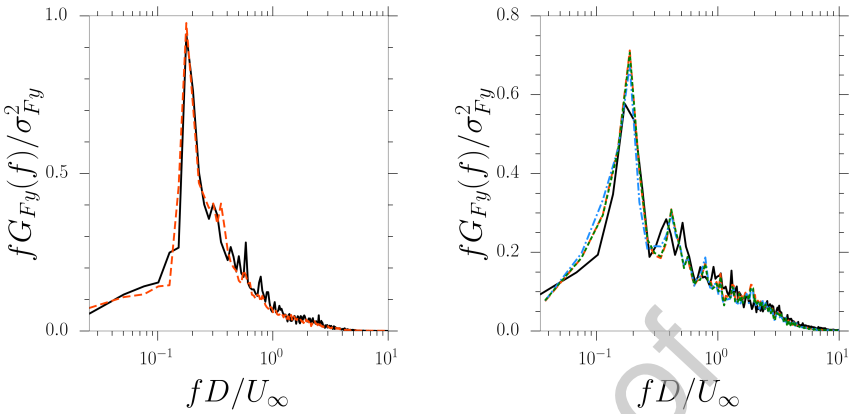

(a) Configuration 1 (b) Configuration 2

Figure 19: PSD of the side loads for the y component, ——: Body-fitted, - - -: Stepwise approach (IB), - - -: S_{ISG} (IB), - - -: S_{PISG} (IB).

namic load for the y and z components. The Power Spectral Density describes how the mean squared value is distributed in frequency:

$$\sigma^2 = \int_0^\infty G(f)df = \int_{-\infty}^{\infty} f \cdot G(f)d\,[log(f)] \tag{10}$$

Therefore, by plotting spectra as $f.G(f)/\sigma^2$ in linear/log axis, one can obtain directly the contribution to the total energy of the considered frequency band. Figures 19(a) and (b) show $f.G_{F_y}(f)/\sigma^2_{F_y}$ of both cases as a function of the Strouhal number $St_D = \frac{fD}{U_\infty}$. The main peaks, located at $St_D = 0.2$ for the first configuration and $St_D = 0.18$ for the second one, are both well reproduced.

4.5. Spectral analysis of fluctuating wall quantities

As reminded by Sagaut and Deck [43], an accurate prediction of r.m.s values does not demonstrate a correct representation of the frequency content. This information is only accessible through a spectral analysis. Such an analysis requires extensive memory storage in order to sample the signal over enough physical time to reach statistical convergence leading to costly simulations. In our cases, the spectral analysis of the wall pressure field required the extraction

of the wall quantities every iteration during 200 ms of physical time to be able to compute the coherence function with a sufficient number of overlapping blocks [56] with Welch's method [61]. Thus, during the simulation, the wall pressure values used to assess the global load were extracted every iteration.

The Power Spectral Densities (PSD) of the fluctuating wall pressure field has been computed with a frequency resolution of 60 Hz. The PSD values are plotted in figure 20 in the streamwise direction to evidence the spatial organisation of the flow dynamics. In order to improve the convergence of the spectral maps, the PSD has been averaged azimuthally for every streamwise location. The IBC simulation accurately reproduces the location of the dominant frequency around $St_D = 0.2$ linked to the vortex shedding phenomenon. Moreover, the low-frequency signal, around $St_D = 0.08$ is well-positioned between the separating point and $X/D = 0.35$. Lastly, a broadband spectrum centred near $St_D = 0.6$ corresponding to the impact of the shear layer structures on the surface of the topology is retrieved on the IBC simulation.

The same analysis has been processed on the second configuration. The results of Weiss and Deck [57] were compared against the present spectral maps in figure 21. The spatial location and the intensity of the fluctuating wall quantities are well assessed by the IB method even for this complex geometry.

In the frame of an axisymmetric afterbody the shedding phenomenon is associated to an antisymmetric mode (m=1) of the pressure field partly responsible of the unsteady side-loads [60, 56]. To assess if this important feature can be computed with an IBC approach, a two-point spectral analysis has been performed to get further into the comparison. More precisely, the azimuthal coherence of two pressure sensors p1(r,x,ϕ_1) and p2(r,x,ϕ_2) located at the same streamwise location x, at a constant radius r and at an azimuthal angle ϕ_i is investigated. Assuming an homogeneous flow, as proposed in [21, 20, 60], the complex coherence function can be expressed as :

$$C(f,r,x,\Delta\phi) = (C_r + jC_i)(f,r,x,\Delta\phi) = \frac{S_{12}(f,r,x,\Delta\phi)}{\sqrt{S_1(f,r,x,\Delta\phi)S_2(f,r,x,\Delta\phi)}} \quad (11)$$

where $j = \sqrt{-1}$, and C_r and C_i are the real and imaginary part of the cross-

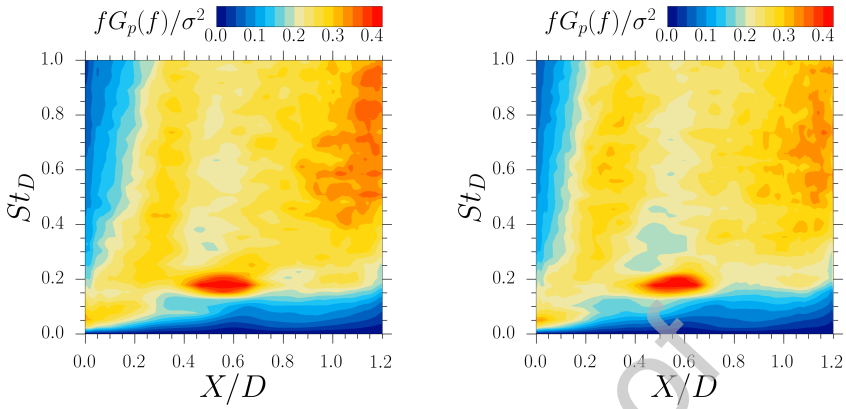

(a) Body-fitted (b) IBC

Figure 20: Maps of the dimensionless Power Spectral Density of the fluctuating wall pressure for every streamwise location along the first configuration.

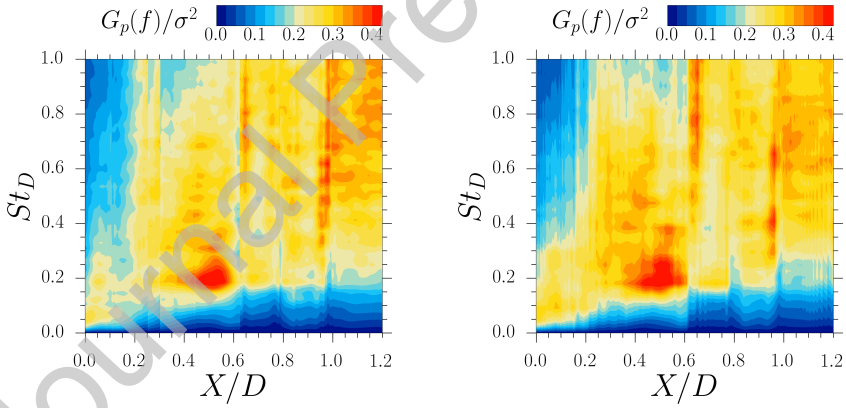

(a) Body-fitted (b) IBC

Figure 21: Maps of the dimensionless Power Spectral Density of the fluctuating wall pressure for every streamwise location along the second configuration.

spectral density function S_{12} and $\Delta\phi$ is the angle between two sensors. Assuming an homogeneous propagation of the disturbance and with $C_i = 0$, C_r is

considered as 2π-periodic and can be expressed as follows:

$$C_r(f,\phi) = \sum_{m=0}^{\infty} C_{r,m}(f) cos(m\Delta\phi) \tag{12}$$

Where $C_{r,m}$ is the percentage of the fluctuating energy at the frequency f relative to the azimuthal mode m with $\sum_m C_{r,m} = 1$. As reminded by Weiss and Deck [56], mode 0 and 1 are characterized respectively by an in-phase and anti-phase signal relation recorded at two angle locations. Hence, the dynamic load phenomena observed on space launcher afterbodies are a consequence of the antisymmetric mode $m = 1$. The spectral maps of this mode are shown in figure 22 for the first configuration and 23 for the second one. For both cases the maximum of the coherence function is to be found at $St_D = 0.2$ and is well-located between $x/D = 0.35$ and $x/D = 0.75$. However, the azimuthal coherence for the dimensionless frequency $St_D = 0.1$ related to the flapping phenomenon has increased between $x/D = 0$ and $x/D = 0.35$ for both simulations with IB.

Such modifications of the azimuthal coherence have also been observed for the first configuration in [56] when four jets were positioned near the beginning of the shear layer in a body-fitted context. The resulting mass flow injection shows the same feature as the present IBC simulation and is a consequence of the non conservativeness of the immersed boundary. This result puts forward the impact of the IB source term on near-wall flows.

This study shows that the IBC method using the new S_{PISG} surface reconstruction permits the analysis of the spatial organization of the fluctuating pressure field and broadens the use hybrid RANS-LES methods for complex geometry simulations.

4.6. Conclusion

The ability of immersed boundary conditions to reproduce all validation levels accessible with body-fitted methodologies has been assessed through the simulation and the comparison of two well-documented test cases. In particular, two methodologies were tested for the "on-the-fly" assessment of global loads

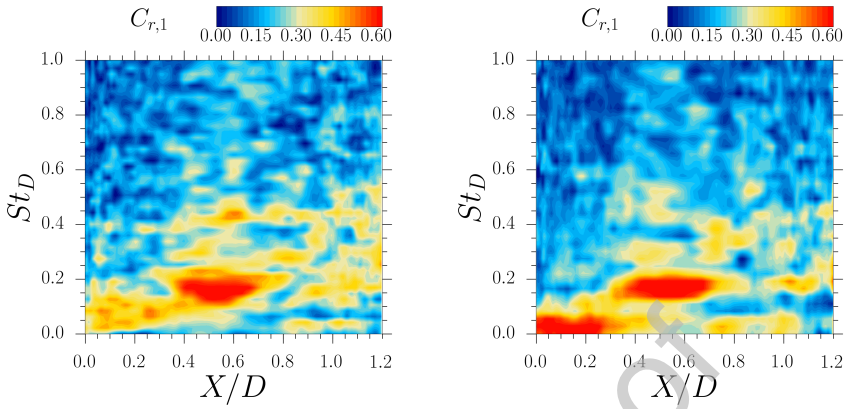

(a) Body-fitted (b) IBC

Figure 22: Maps of the azimuthal pressure mode $C_{r,1}$ for every streamwise location along configuration 1.

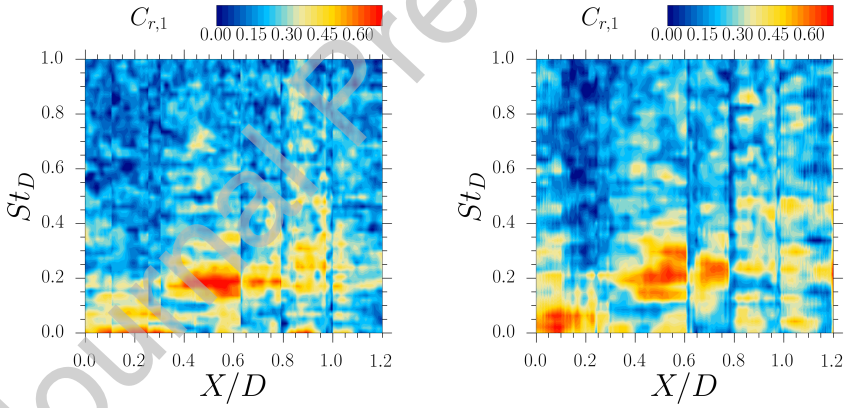

(a) Body-fitted (b) IBC

Figure 23: Maps of the azimuthal pressure mode $C_{r,1}$ for every streamwise location along configuration 2.

on immersed bodies. The method based on a stepwise representation of the surface has shown its capacity and its numerical simplicity to perform a fast evaluation of these quantities. Nevertheless, the present generalised methodology for the generation of surface meshes on IBC permits to perform the same

post-processing as with body-fitted methods without extra computational cost during the simulations. Moreover, this strategy allows the extraction of wall quantities on IB which permits to achieve high validation levels such as single and two-point spectral analyses. Following the classification of Sagaut and Deck [43], the validation levels from 0 to 5 (i.e. from integral efforts to cross-spectral analysis) have been performed successfully on IBC and compared to body-fitted simulations using the same numerical methods and showed the capacity of IBC to accurately model wall conditions even for high Reynolds number flows. However, the two-point spectral analysis reveals the impact of the IBC forcing on the wall quantities for the lowest frequencies. Indeed, the occurrence of spurious low frequencies acts as an injection of momentum in the simulation, which highlights the impact of the source terms used to create the boundary condition. Nonetheless, the present strategy combining ZDES and the zonal use of IBC (ZIBC) has shown its capacity to accurately assess the impact of the pressure fluctuation on space launcher afterbodies while reducing dramatically the initial preprocessing step required for full body-fitted simulations.

Appendix A. Algorithm for the extraction of wall quantities from structured grids

The cells in structured grids are defined by three indexes (i,j,k) (e.g. streamwise, wall-normal, spanwise/azumutal directions). For body-fitted approaches, wall cells are located at the edge of a computational domain, and consequently one of these indexes is a constant. Hence, the extraction of wall cells results in 2D structured files. While unstructured data require a connectivity table, the spatial organisation of structured data is implicitly known by the indexes. For IBC, the forcing points do not generally lie on the faces of the computational domain. Therefore we proposed to create a new index $\tilde{\imath}$ to replace two indexes in order to create 2D indexed extractions for IBC. In the present case the index j has been "unfolded" in the i index direction to create $\tilde{\imath}$ as presented in figure A.24. This first step produced a different number of $\tilde{\imath}$ for every k. Therefore the spatial organisation of the structured indexes is not preserved so far. For a given i, if the number of cells is different between k index, it will result in an offset in the spatial organisation of the indexes (see figure A.25).

To avoid any offset between $\tilde{\imath}$ and k, the same number of cells has to be written for a given i index for every k. This number corresponds to the maximum number of cells unfolded at an index i for every k. If the number of cells is lower than this maximum number, the last cell is added multiple times. The addition of these cells, represented in green in A.24, preserves the connectivity in k of the cells. Figure A.25 presents a 3D application of this method on the configuration 2.

The final data file contains a 2D structured surface mesh linking every IB forcing points. This structured grid can be used as the previous one for load integration and extraction. One could argue that the multiplication of several cells could result in an incorrect surface computation and therefore an incorrect load computation. Since the duplicated cells have the same coordinates, the integration surface remains unchanged.

This method is useful for geometries aligned in one particular index direc-

tion. For some applications, the number of added cells will counterbalance the advantage to use structured extraction. Nonetheless, for the present cases, this methodology provides structured data with less than 50 additional cells and allows a direct comparison with wall extractions realised on body-fitted structured grids.

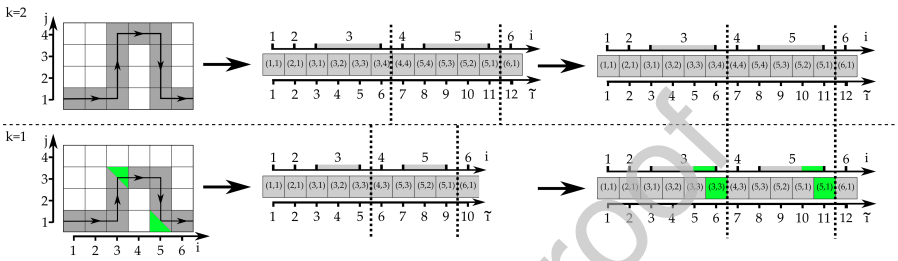

Figure A.24: Two-dimensional sketches of the structured extraction procedure. Initial structured-grid information (Left)/ Surface unfolding (Center) / Surface filling (Right).

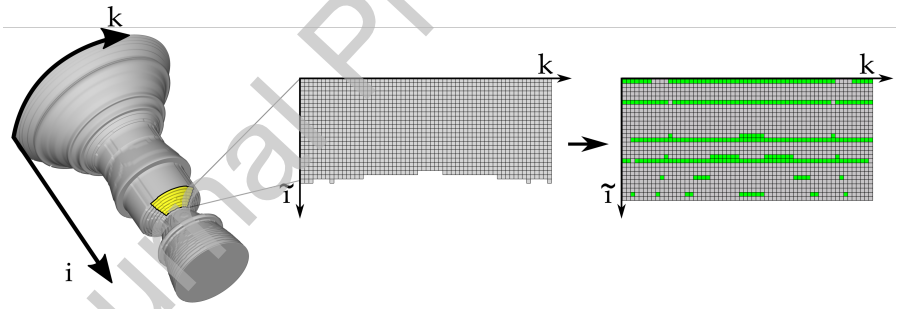

Figure A.25: Three-dimensional sketches of the structured extraction procedure. Initial structured-grid information (Left)/ Surface unfolding (Center) / Surface filling (Right).

References

[1] Balaras, E., 2004. Modeling complex boundaries using an external force field on fixed Cartesian grids in large-eddy simulations. Computers & Fluids 33 (3), 375–404.

[2] Bernardini, M., Modesti, D., Pirozzoli, S., 2016. On the suitability of the immersed boundary method for the simulation of high-reynolds-number separated turbulent flows. Computers & Fluids 130, 84–93.

[3] Bharadwaj S, A., Ghosh, S., Jan. 2020. Data reconstruction at surface in immersed-boundary methods. Computers & Fluids 196, 104236.

[4] Brehm, C., Barad, M. F., Kiris, C. C., 2016. An immersed boundary method for solving the compressible navier-stokes equations with fluid-structure interaction. In: 54th AIAA Aerospace Sciences Meeting.

[5] Brehm, C., Barad, M. F., Kiris, C. C., 2016. Towards a viscous wall model for immersed boundary methods. In: 46th AIAA Fluid Dynamics Conference.

[6] Byun, D. Y., Baek, S. W., Kim, M. Y., Jun. 2003. Investigation of radiative heat transfer in complex geometries using blocked-off, multiblock, and embedded boundary treatments. Numerical Heat Transfer, Part A: Applications 43 (8), 807–825.

[7] Capizzano, F., 2007. A compressible flow simulation system based on cartesian grids with anisotropic refinements. In: 45th AIAA Aerospace Sciences Meeting and Exhibit.

[8] Capizzano, F., 2016. Coupling a wall diffusion model with an immersed boundary technique. AIAA Journal 54 (2), 728–734.

[9] Capizzano, F., sep 2017. Automatic generation of locally refined cartesian meshes: Data management and algorithms. International Journal for Numerical Methods in Engineering 113 (5), 789–813.

[10] Chen, Z. L., Hickel, S., Devesa, A., Berland, J., Adams, N. A., 2014. Wall modeling for implicit large-eddy simulation and immersed-interface methods. Theoretical and Computational Fluid Dynamics 28, 1–21.

[11] Cristallo, A., Verzicco, R., sep 2006. Combined immersed boundary/large-eddy-simulations of incompressible three dimensional complex flows. Flow, Turbulence and Combustion 77 (1-4), 3–26.

[12] Dairay, T., Lamballais, E., Benhamadouche, S., oct 2017. Mesh node distribution in terms of wall distance for large-eddy simulation of wall-bounded flows. Flow, Turbulence and Combustion 100 (3), 617–626.

[13] de Tullio, M., Palma, P. D., Iaccarino, G., Pascazio, G., Napolitano, M., aug 2007. An immersed boundary method for compressible flows using local grid refinement. Journal of Computational Physics 225 (2), 2098–2117.

[14] Deck, S., jul 2005. Numerical simulation of transonic buffet over a supercritical airfoil. AIAA Journal 43 (7), 1556–1566.

[15] Deck, S., 2012. Recent improvements in the Zonal Detached Eddy Simulation (ZDES) formulation. Theoretical and Computational Fluid Dynamics 26 (6), 523–550.

[16] Deck, S., Gand, F., Brunet, V., Khelil, S. B., jul 2014. High-fidelity simulations of unsteady civil aircraft aerodynamics: stakes and perspectives. application of zonal detached eddy simulation. Philosophical Transactions of the Royal Society A: Mathematical, Physical and Engineering Sciences 372 (2022), 20130325–20130325.

[17] Deck, S., Laraufie, R., sep 2013. Numerical investigation of the flow dynamics past a three-element aerofoil. Journal of Fluid Mechanics 732, 401–444.

[18] Deck, S., Nguyen, A. T., 2004. Unsteady side loads in a thrust-optimized contour nozzle at hysteresis regime. AIAA Journal 42, 1878–1888.

[19] Deck, S., Renard, N., 2020. Towards an enhanced protection of attached boundary layers in hybrid rans/les methods. Journal of Computational Physics 400.

[20] Deck, S., Thorigny, P., 2007. Unsteadiness of an axisymmetric separating-reataching flow: Numerical investigation. Physics of Fluids 19 (065103), 1–20.

[21] Deprés, D., Reijasse, P., Dussauge, J. P., 2004. Analysis of unsteadiness in afterbody transonic flows. AIAA Journal 42 (12), 2541–2550.

[22] Fadlun, E., Verzicco, R., Orlandi, P., Mohd-Yusof, J., 2000. Combined immersed-boundary finite-difference methods for three-dimensional complex flow simulations. Journal of Computational Physics 161 (1), 35–60.

[23] Gear, C. W., mar 1971. Algorithm 407: DIFSUB for solution of ordinary differential equations [d2]. Communications of the ACM 14 (3), 185–190.

[24] Ghias, R., Mittal, R., Dong, H., 2007. A sharp interface immersed boundary method for compressible viscous flows. Journal of Compultational Physics 225, 528–553.

[25] Kim, W., Lee, I., Choi, H., apr 2018. A weak-coupling immersed boundary method for fluid–structure interaction with low density ratio of solid to fluid. Journal of Computational Physics 359, 296–311.

[26] Kiris, C. C., Housman, J. A., Barad, M. F., Brehm, C., Sozer, E., Moini-Yekta, S., 2016. Computational framework for launch, ascent, and vehicle aerodynamics (lava). Aerospace Science and Technology 55, 189–219.

[27] Liou, M.-S., 1996. A sequel to AUSM: AUSM+. Journal of Computational Physics 129, 364382.

[28] Meliga, P., Reijasse, P., 2007. Unsteady transonic flow behind an axisymmetric afterbody with two boosters. In: Proceeding of the 25th AIAA Applied Aerodynamics Conference Miami. pp. 1–8.

[29] Merlin, C., Domingo, P., Vervisch, L., 2013. Immersed boundaries in large eddy simulation of compressible flows. Flow Turbulence Combust 90, 29–68.

[30] Meyer, M., Devesa, A., Hickel, S., Hu, X., Adams, N., sep 2010. A conservative immersed interface method for large-eddy simulation of incompressible flows. Journal of Computational Physics 229 (18), 6300–6317.

[31] Meyer, M., Hickel, S., Adams, N., jun 2010. Assessment of implicit large-eddy simulation with a conservative immersed interface method for turbulent cylinder flow. International Journal of Heat and Fluid Flow 31 (3), 368–377.

[32] Mittal, R., Iaccarino, G., 2005. Immersed boundary methods. Annual Review of Fluid Mechanics 37, 239–261.

[33] Mizuno, Y., Takahashi, S., Nonomura, T., Nagata, T., Fukuda, K., 2015. A simple immersed boundary method for compressible flow simulation around a stationary and moving sphere. Mathematical Problems in Engineering 2015, 1–17.

[34] Mochel, L., 2015. Etude des effets technologiques par des méthodes numériques innovantes sur des configurations de lanceur. Ph.D. thesis, Universit Pierre et Marie Curie - Paris VI.

[35] Mochel, L., Weiss, P.-É., Deck, S., 2014. Zonal immersed boundary conditions: Application to a high-Reynolds-number afterbody flow. AIAA Journal 52 (12), 27822794.

[36] Mohd-Yusof, J., 1997. Combined immersed-boundary/b-spline methods for simulations of flows in complex geometries. Annual Research Briefs Center for Turbulence Research, 313–328.

[37] Nam, J., Lien, F., jun 2015. Assessment of ghost-cell based cut-cell method for large-eddy simulations of compressible flows at high Reynolds number. International Journal of Heat and Fluid Flow 53, 1–14.

[38] O'Brien, A., Bussmann, M., mar 2018. A volume-of-fluid ghost-cell immersed boundary method for multiphase flows with contact line dynamics. Computers & Fluids 165, 43–53.

[39] Pain, R., Weiss, P.-É., Deck, S., sep 2014. Zonal detached eddy simulation of the flow around a simplified launcher afterbody. AIAA Journal 52 (9), 1967–1979.

[40] Pain, R., Weiss, P.-É., Deck, S., Robinet, J.-C., 2019. Large scale dynamics of a high reynolds number axisymmetric separating/reattaching flow. Physics of Fluids 31 (12), 125119.

[41] Peskin, C. S., 1972. Flow patterns around heart valves: a numerical method. Journal of Computational Physics 10 (2), 252–271.

[42] Piquet, A., Roussel, O., Hadjadj, A., 2016. A comparative study of brinkman penalization and direct-forcing immersed boundary methods for compressible viscous flows. Computers & Fluids 136, 272–284.

[43] Sagaut, P., Deck, S., jun 2009. Large eddy simulation for aerodynamics: status and perspectives. Philosophical Transactions of the Royal Society A: Mathematical, Physical and Engineering Sciences 367 (1899), 2849–2860.

[44] Sedaghat, M. H., Shahmardan, M. M., Norouzi, M., Jayathilake, P. G., Nazari, M., 2016. Numerical simulation of muco-ciliary clearance: immersed boundary lattice boltzmann method. Computers & Fluids 131, 91–101.

[45] Simon, F., Deck, S., Guillen, P., Sagaut, P., nov 2006. Reynolds-averaged navier-stokes/large-eddy simulations of supersonic base flow. AIAA Journal 44 (11), 2578–2590.

[46] Slotnick, J., Khidadoust, A., Alonso, J., Darmofal, D., Gropp, W., Lurie, E., Mavriplis, D., 2013. Cfd vision 2030 study: a path to revolutionary computational aerosciences. Tech. Rep. 23681-2199, NASA Langley Research Center.

[47] Specklin, M., Delauré, Y., jul 2018. A sharp immersed boundary method based on penalization and its application to moving boundaries and turbulent rotating flows. European Journal of Mechanics - B/Fluids 70, 130–147.

[48] Syrakos, A., Varchanis, S., Dimakopoulos, Y., Goulas, A., Tsamopoulos, J., dec 2017. A critical analysis of some popular methods for the discretisation of the gradient operator in finite volume methods. Physics of Fluids 29 (12), 127103.

[49] Tamaki, Y., Harada, M., Imamura, T., 2017. Near-wall modification of Spalart-Allmaras turbulence model for immersed boundary method. AIAA Journal 55 (9), 3027–3039.

[50] Tamaki, Y., Imamura, T., jun 2017. Turbulent flow simulations of the NASA common research model using the immersed boundary method with a wall function. In: 35th AIAA Applied Aerodynamics Conference. American Institute of Aeronautics and Astronautics.

[51] Tamaki, Y., Imamura, T., apr 2018. Turbulent flow simulations of the common research model using immersed boundary method. AIAA Journal, 1–12.

[52] Tyacke, J. C., Mahak, M., Tucker, P. G., 2016. Large-scale multifidelity, multiphysics, hybrid Reynolds-Averaged Navier-Stokes/Large-Eddy Simulation of an installed aeroengine. Journal of Propulsion and Power 32 (4), 997–1008.

[53] Tyliszczak, A., Ksiezyk, M., mar 2018. Large eddy simulations of wall-bounded flows using a simplified immersed boundary method and high-order compact schemes. International Journal for Numerical Methods in Fluids.

[54] Wald, I., Havran, V., sep 2006. On building fast kd-trees for ray tracing, and on doing that in o(n log n). In: 2006 IEEE Symposium on Interactive Ray Tracing. IEEE.

[55] Wang, K., Rallu, A., Gerbeau, J.-F., Farhat, C., 2011. Algorithms for interface treatment and load computation in embedded boundary methods

for fluid and fluid-structure interaction problems. International Journal for Numerical Methods in Fluids 67, 1175–1206.

[56] Weiss, P.-É., Deck, S., 2011. Control of the antisymmetric mode (m =1) for high Reynolds axisymmetric turbulent separating/reattaching flows. Physics of Fluids 23, 095102.

[57] Weiss, P.-É., Deck, S., 2011. Zonal detached eddy simulation of the flow dynamics on an Ariane 5-type afterbody. In: 4th Eur. Conf. for Aerospace Sciences, St-Petersburg, Russia (2011).

[58] Weiss, P. É., Deck, S., jul 2013. Numerical investigation of the robustness of an axisymmetric separating/reattaching flow to an external perturbation using ZDES. Flow, Turbulence and Combustion 91 (3), 697–715.

[59] Weiss, P.-É., Deck, S., nov 2018. On the coupling of a zonal body-fitted/immersed boundary method with ZDES: Application to the interactions on a realistic space launcher afterbody flow. Computers & Fluids 176, 338–352.

[60] Weiss, P.-É., Deck, S., Robinet, J.-C., Sagaut, P., 2009. On the dynamics of axisymmetric turbulent separating/reattaching flows. Physics of Fluids 21 (075103), 1–8.

[61] Welch, P., Jun. 1967. The use of fast fourier transform for the estimation of power spectra: A method based on time averaging over short, modified periodograms. IEEE Transactions on Audio and Electroacoustics 15 (2), 70–73.

[62] Wilhelm, S., Jacob, J., Sagaut, P., jun 2018. An explicit power-law-based wall model for lattice Boltzmann method-Reynolds-averaged numerical simulations of the flow around airfoils. Physics of Fluids 30 (6), 065111.

[63] Yang, J., Balaras, E., jun 2006. An embedded-boundary formulation for large-eddy simulation of turbulent flows interacting with moving boundaries. Journal of Computational Physics 215 (1), 12–40.

[64] Yang, J., Stern, F., 2012. A simple and efficient direct forcing immersed boundary framework for fluidstructure interactions. Journal of Computational Physics 231, 5029–5061.

[65] Zhou, C. H., 2017. Rans simulation of high-Re turbulent flows using an immersed boundary method in conjunction with wall modeling. Computers & Fluids 143, 73–89.

Declaration of interests

☒ The authors declare that they have no known competing financial interests or personal relationships that could have appeared to influence the work reported in this paper.

☐The authors declare the following financial interests/personal relationships which may be considered as potential competing interests:

CRediT author statement

(C&F, Manueco, Weiss, Deck, 2020)

Lucas Manueco:

Conceptualization, Methodology, Software, Validation, Investigation, Resources, Data Curation, Writing - Original Draft, Writing - Review & Editing, Visualization

Pierre-Elie Weiss:

Conceptualization, Formal analysis, Investigation, Resources, Writing - Review & Editing, Visualization, Supervision, Project administration, Funding acquisition

Sébastien Deck:

Conceptualization, Formal analysis, Investigation, Resources, Writing - Review & Editing, Visualization, Supervision, Project administration, Funding acquisition